SLAC–PUB–15973
June 4, 2014

Measurements of High-Intensity Laser Induced Ionizing Radiation at SLAC

Taiee Liang[1,2], Johannes Bauer[1], Maranda Cimeno[1], Anna Ferrari[3], Eric Galtier[1], Eduardo Granados[1], James Liu[1], Bob Nagler[1], Alyssa Prinz[1], Sayed Rokni[1], Henry Tran[1], Mike Woods[1]

[1]*SLAC National Accelerator Laboratory, Menlo Park, CA USA*
[2]*Georgia Institute of Technology, Atlanta, GA USA*
[3]*Institute of Radiation Physics, Dresden, Germany*

A systematic study of measurements of photon and neutron radiation doses generated in high-intensity laser-target interactions is underway at SLAC National Accelerator Laboratory using femtosecond pulsed Ti:sapphire laser (800 nm, 40 fs, up to 1 J and 25 TW) at the Linac Coherent Light Source's (LCLS) Matter in Extreme Conditions (MEC) facility. Preliminary results from recent measurements with the laser-optic target system (peak intensity 1.8×10^{18} W/cm^2) are presented and compared with results from calculations based on analytical models and FLUKA Monte Carlo simulations.

SUBMITTED TO

Proceedings of SATIF-12
Fermi National Accelerator Laboratory
Batavia, IL USA, April 28–30, 2014

[1]Work supported by the U.S. Department of Energy, under contract DE–AC02–76–SFO0515.

1 Introduction

The number and use of high intensity (multi-terawatt and petawatt) lasers in research facilities has seen a rapid rise in recent years. These lasers can now be used in conjunction with research programs in 3rd and 4th generation light sources to study matter under extreme conditions [1], or as sources of particle acceleration [2].

High-intensity laser-matter interaction in vacuum can create a plasma, and further laser interactions with the plasma can accelerate electrons in the plasma up to 10s to 1000s of keV [3–9]. These "hot" electrons will interact with the laser target and the target chamber and generate bremsstrahlung X-rays [10, 11]. This mixed field of electrons and photons can be a source of ionizing radiation hazard for personnel working on or near such systems if sufficient radiological controls are not implemented. Currently, there is limited information on the ionizing radiation hazards associated with such laser-matter interactions, and on controls for such hazards. Characterization of the radiation source term, understanding the radiological hazards, and development of appropriate measures to ensure personnel safety in this rapidly rising field are needed.

SLAC Radiation Protection (RP) Department, in conjunction with the Linac Coherent Light Source (LCLS) Laser Division, has embarked on a systematic study to measure ionizing radiation under controlled experiments using the high-intensity, short-pulse laser of the LCLSs Matter in Extreme Conditions (MEC) instrument [12].

As part of this on-going effort, SLAC RP has also been developing analytical models to estimate radiation yield (Sv/J) and performing Monte Carlo simulations to characterize the measured data more accurately [13–16]. Another goal from the measurements is to evaluate the performance of various types of active and passive detectors in the laser-induced radiation fields. Evaluation of the efficacy of shielding for protection of personnel from the ionizing radiation and development of accurate methods and tools to estimate the required shielding at various intensities for different targets is the overarching purpose of these studies.

Experiments performed to-date include radiation measurements at the Lawrence Livermore National Laboratory's (LLNL) Titan laser facility in 2011 and measurements at SLACs MEC facility in 2012 and 2014. In the Titan measurements, the laser beam intensity and pulse energy were $\sim 10^{20}$ W/cm^2 and 400 J, respectively. Targets included 3-5 mm thick hydrocarbon foam and 1 mm gold foil. The 2012 experiment at SLAC's MEC laser facility was performed with laser intensities between 3×10^{16} and 6×10^{17} W/cm^2 (40 fs and up to 0.15 J per pulse). Targets for the MEC 2012 experiment included gold foils (0.01 and 0.1 mm) and copper (1 mm). The results of these two measurements have been reported elsewhere [14, 16]. Preliminary results of the latest MEC experiment in February 2014 are reported here and are compared with results from analytical models and Monte Carlo simulations.

2 SLAC RP Dose Model

The bremsstrahlung photon yield due to hot electrons generated from laser-matter interaction is characterized by the temperature (or energy) of hot electrons, T_h, and the laser energy to electron energy conversion efficiency, α. The hot electron temperature T_h is a function of laser parameters and increases with the normalized laser intensity, $I\lambda^2$, where I (W/cm^2) is the laser intensity, λ the laser wavelength (μm) [17, 18].

2.1 Electron Temperature and Energy Distribution

At lower laser intensities, inverse bremsstrahlung and resonance absorption are the dominant mechanisms for producing hot electrons, and SLAC RP uses Meyerhofer's empirical scaling of Equation 1 to calculate T_h in units of keV for a normalized laser intensity $I\lambda^2 < 1.6 \times 10^{17}$ W-μm^2/cm^2 [17].

$$T_h = 6 \times 10^{-5} (I\lambda^2)^{\frac{1}{3}} \tag{1}$$

At higher laser intensities, when $I\lambda^2 \geq 1.6 \times 10^{17}$ W-μm^2/cm^2, the ponderomotive force is the primary electron heating mechanism, and it is defined as the force that a dipole experiences in an oscillating electromagnetic field. In the case of a laser-plasma interaction, the free electrons in the plasma experience the oscillating electric field of the incident laser. Equation 2 is used to calculate T_h based on the ponderomotive force where M_e is the electron rest mass (511 keV) [18, 19].

$$T_h = M_e \left(-1.0 + \sqrt{1.0 + \frac{I\lambda^2}{1.37 \times 10^{18}}} \right) \tag{2}$$

Figure 1 shows the distinct inflection point at $I\lambda^2 = 1.6 \times 10^{17}$ W-μm^2/cm^2 from the combination of Equations 1 and 2 for calculating T_h. The photon dose is proportional to a power of T_h and is generated through bremsstrahlung of hot electrons with the laser's target and target chamber's walls. The SLAC RP model for T_h provides a conservative approach at estimating the photon dose yield from laser-matter interaction.

The energy distribution of electrons is also characterized by T_h. Equations 3 and 4 give two distributions used by RP to characterize the energy of the hot electrons for I below and above 10^{18} W/cm^2, respectively [20–22]. The Relativistic Maxwellian case with an average electron energy of $3T_h$ is a harder electron spectrum than the Maxwellian case with an average energy of $1.5T_h$.

$$\text{Maxwellian} : N_e \propto E_e^{1/2} \, e^{-E_e/T_h} \text{ for } I \leq 10^{18} \text{ W/cm}^2 \tag{3}$$

$$\text{Relativistic Maxwellian} : N_e \propto E_e^{2} \quad e^{-E_e/T_h} \text{ for } I > 10^{18} \text{ W/cm}^2 \tag{4}$$

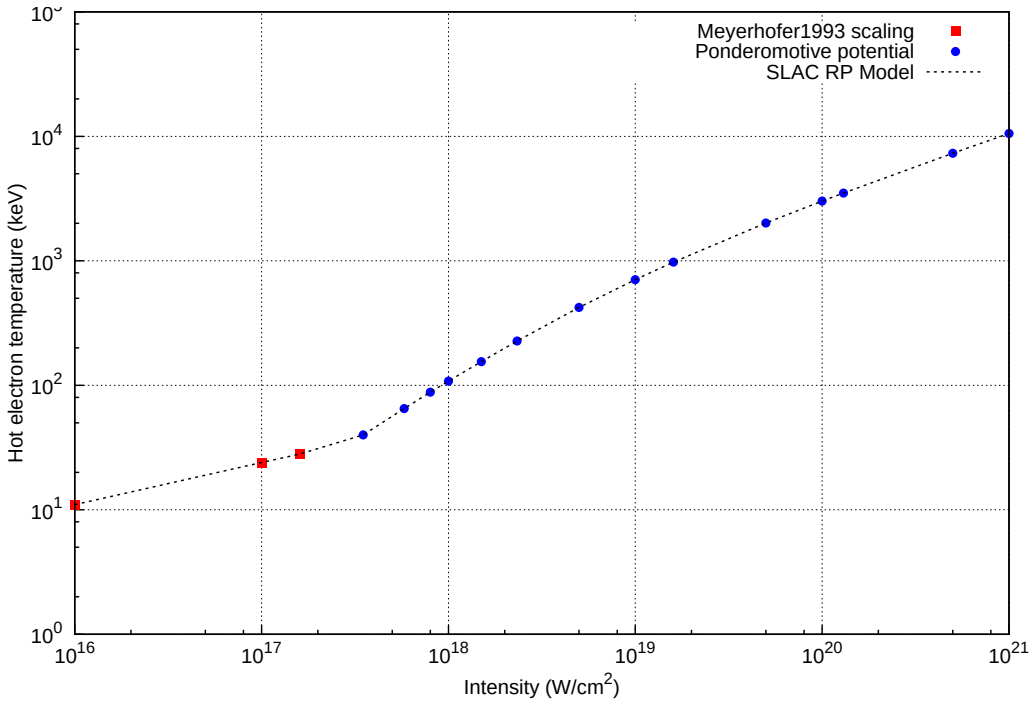

Figure 1: SLAC RP model for T_h (keV) as a function of I (W/cm^2) with $\lambda = 0.8$ μm

2.2 Photon Dose Calculation

Monte Carlo codes such as FLUKA can predict the photon dose from a hot electron spectrum described by Equation 3 or 4, the hot electron temperature T_h, the laser energy to electron energy conversion efficiency α, and the angular and spatial distribution of the electrons. However, it is desired to have a simple empirical formula based on the above parameters that can provide a quick estimate of the photon dose yield due to laser-matter interaction.

The SLAC RP model for photon dose utilizes Equations 5 and 6 from Y. Hayashi [23] that are derived for the maximum bremsstrahlung photon dose (occurring at 0° along laser axis) generated through interaction between a short pulse high-power laser and a solid target. The equations are based on a laser-generated electron spectrum with a Relativistic Maxwellian distribution as described earlier in Equation 4.

$$H_x \approx 1.8 \times \left(1.10 \times \frac{\alpha}{R^2}\right) \times T_h^2 \qquad (T_h < 3 \text{ MeV}) \tag{5}$$

$$H_x \approx 1.8 \times \left(3.32 \times \frac{\alpha}{R^2}\right) \times T_h \qquad (T_h \geq 3 \text{ MeV}) \tag{6}$$

The 0° photon dose yield H_x is in units of Sv/J, and R is the distance between the laser-target interaction point and the dose point in cm. Equations 5 and 6 from

Hayashi were derived based only on the ponderomotive force theory for I between 10^{19} to 10^{21} W/cm^2. To adapt for lower laser intensities, the RP model uses the T_h from Equations 1 and 2 to calculate H_x. The SLAC RP model for the laser conversion efficiency α is 30% for $I \leq 10^{19}$ W/cm^2 and 50% for $I > 10^{19}$ W/cm^2 [12,24]. Because Hayashi's equations only account for the 0° photon dose yield at very high-intensity lasers with no shielding, the SLAC RP model may overestimate the photon dose outside of 00° and when accounting for the shielding effects of the target chamber itself.

3 Experimental Setup and Beam Parameters

The February 2014 experiment was performed at the LCLS Hutch 6 (MEC hutch) using the 0.8 μm Ti:sapphire short pulse laser on a 100 μm thick copper target. Figure 2 shows the layout of MEC Hutch 6 with its short and long pulse laser systems and the aluminum target chamber.

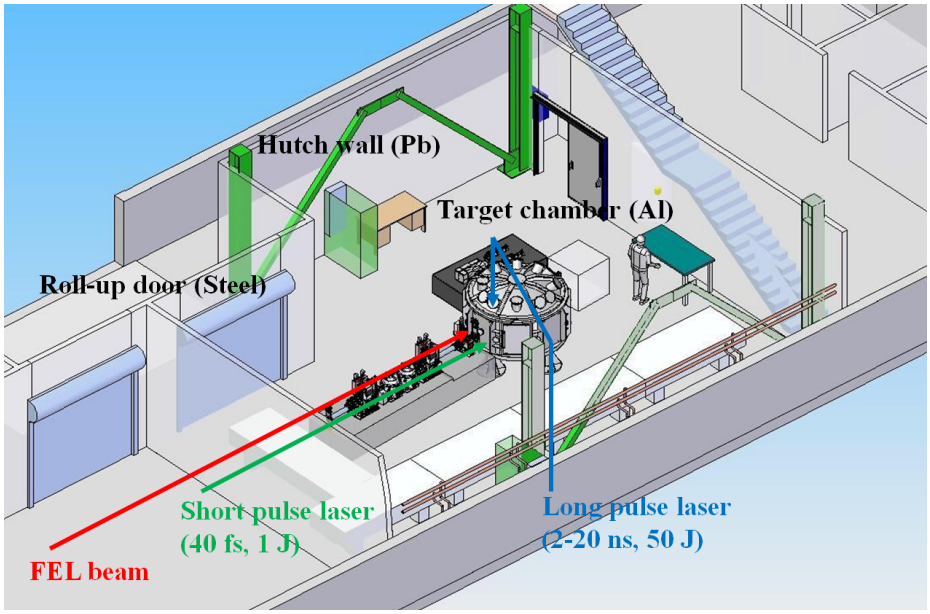

Figure 2: Layout of SLAC LCLS Hutch 6

3.1 MEC Target Chamber Layout

Figure 3 shows a horizontal cross section of the MEC target chamber. The target chamber has a radius of about 1 meter, and its aluminum walls vary in thickness, but are typically 2.54 cm thick (5.08 cm for chamber doors). For the 2014 MEC experiment described here, the unfocused short pulse laser entered the target chamber from

the left and was directed with a series of mirrors to an Al-coated off-axis parabolic (OAP) mirror. The OAP mirror focused the laser beam to a horizontal and vertical $1/e^2$ radius spot size of 13×8 μm^2 with a peak intensity of 1.8×10^{18} W/cm^2 at 192 mJ. The focused laser beam was incident on the target material at an angle of 15° relative to target normal. Copper foils of thickness 100 μm served as the laser targets and were positioned at the chamber center and perpendicular to the FEL axis.

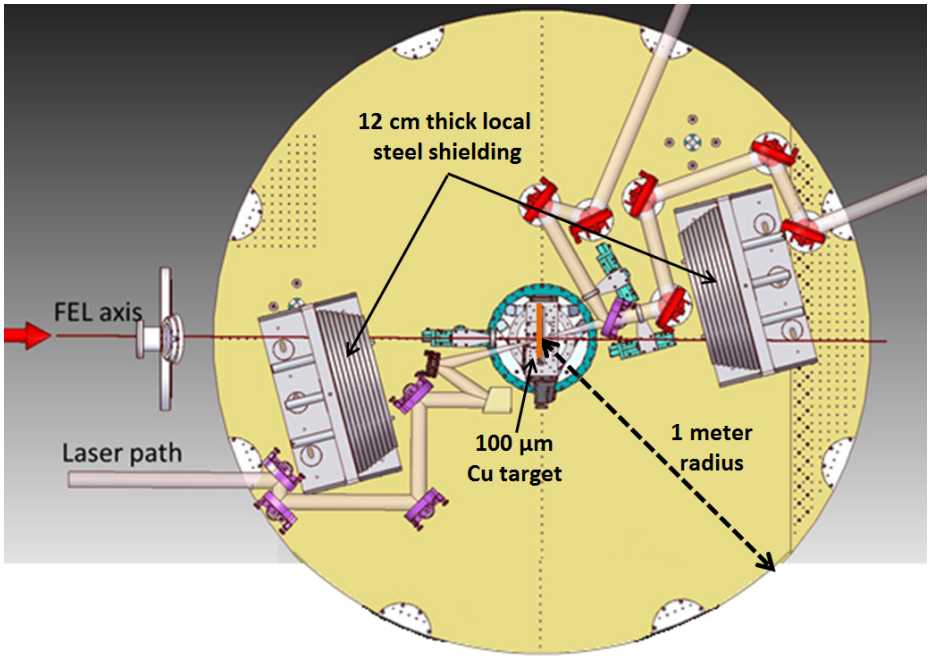

Figure 3: Layout of SLAC LCLS Hutch 6

The lenses and mirrors located downstream of the laser-matter interaction point were used before the start of the experiment for characterizing laser beam parameters. Pulse energy measurements were taken with a Coherent J50 50M-IR sensor and a Coherent LabMax-TOP meter. The pulse duration was measured twice with two separate instruments, a Coherent single-shot autocorrelator (SSA) and an APE LX Spider autocorrelator, before and after the experiment, and both instruments reported the same result. An Adimec OPAL-1000 CCD camera, calibrated before the experiment, determined the spot size by imaging the beam. The measured profile of the focused beam on target was a complicated distribution with multiple peaks, and this contributes to the uncertainty associated with laser intensity calculations.

With the laser system operating at 1 Hz, a target rastering system ensured each laser shot interacted with fresh copper material. Furthermore, as seen in Figure 3, two 12 cm thick steel shields were deployed inside the MEC chamber in the forward and backward direction of the laser beam to evaluate their effectiveness at shielding

the generated ionizing radiation. Their efficacy is discussed later in the measurement results.

Table 1 lists key laser and optic parameters for the experiment and their associated uncertainties (one standard deviation). A total of 540 laser shots on target were taken during the course of the experiment. Due to the damage to the Al-coated OAP focusing mirror from the high-energy laser beam, only a limited number of shots could be taken. Future experiments using the MEC laser system will utilize other metal mirror coatings with higher reflectivity.

Parameters	MEC 2014
target material	Copper
target thickness (μm)	100
energy before compressor (mJ)	1400 (5%)
transmission fraction compressor	0.68 (2%)
transmission fraction of focusing mirror	0.87 (5%)
fraction of energy in main peak	0.23 (20%)
energy on target in main peak (mJ)	192 (21%)
FWHM pulse duration (fs)	70 (5%)
horizontal $1/e^2$ radius spot size of main peak (μm)	13 (10%)
vertical $1/e^2$ radius spot size of main peak (μm)	8 (10%)
calculated peak intensity (W/cm^2)	1.8×10^{18} (27%)

Table 1: Parameters from February 2014 MEC experiment (uncertainties in parentheses)

3.2 Detectors and Instruments

A combination of passive dosimeters and active detectors were deployed inside and outside of the Al MEC target chamber and around Hutch 6 for radiation measurements. The passive dosimeters included electrostatic pocket ion chambers (PIC) with a full scale of 0.02 or 2 mSv and Landauer personnel dosimeters (nanoDot, Luxel+ Ja, and InLight). Only nanoDots were approved for use in the MEC under vacuum conditions, and these were expected to record high dose values from the mixed electron and photon field inside the target chamber. All other dosimeters (0.02 and 2 mSv PICs, Luxel+ Ja, and Inlight) were deployed outside the target chamber to measure the photon doses that escape the target chamber.

The active instruments included RADOS electronic dosimeters, two HPI-6031 styrofoam-walled ion chambers, two PTW-7262 pressurized argon ion chambers, Victoreen 451 handheld ion chambers, and two polyethylene-moderated BF_3 neutron detectors (a quasi-remmeter design). The RADOS were added to the passive dosimeters

outside the target chamber at their respective locations. The two HPI ion chambers, HPI-01 and HPI-02, were positioned directly outside the target chamber. One of the PTW ion chambers, PTW-01, was located in the Hutch 6 control room on the roof, the other, PTW-02, was at the Hutch 6 steel roll up door. The Victoreen 451 meters and BF_3 detectors were deployed at various angles and distances around the target chamber. The active instruments provided real-time dose monitoring information throughout the experiment. These detectors are described in detail elsewhere [16].

4 Measurement Results

The amount of ionizing radiation generated from laser-matter interaction depends heavily on the intensity and energy of laser and less on the solid target material and thickness. For a laser interacting with a solid high Z target, the radiation field inside the target chamber is composed of the accelerated hot electrons and bremsstrahlung photons originating from either the copper target itself or the walls of the Al chamber. The varying 2.54 to 5.08 cm thick Al wall of the target chamber is expected to attenuate the large majority of the low energy electrons and photons. However, electrons and photons of sufficiently high energy can penetrate the wall, or the chamber's thin 5 mm glass view ports. The following sections provide preliminary measurements results from active and passive detectors used during the MEC experiment.

4.1 Dose Inside Target Chamber

Passive nanoDot dosimeters inside the MEC chamber measured very high integrated doses from the experiment. The nanoDot results presented here are based on Kr-85 shallow dose calibration that accounts for the high fluence electron field inside the chamber. Figure 4 presents a polar plot of dose from nanoDots located 30 cm radially from the laser-target interaction point.

The maximum measured dose is 650 cGy in the backward direction and 100 cGy in the forward. The angular distribution of dose suggests that the dose is peaked towards 0°, whereas the dose in the backward direction spreads over a wide angle. Two possible factors may contribute to the difference between the measured forward and backward dose: target thickness and laser intensity. Studies at other facilities have shown that the dose is dominantly in the forward direction [25]. However, these studies utilize filters to measure only electrons of 100 keV and greater, or they use a very high laser intensity between $10^{19} - 10^{20}$ W/cm^2. On the other hand, the February 2014 MEC measurements presented here include dose from low energy electrons along with high energy, and the laser intensity is also comparatively low at 1.8×10^{18} W/cm^2. In addition, the 100 μm thick copper target used in this experiment can be considered a thick target shielding to low energy electrons in the forward direction. This shows the

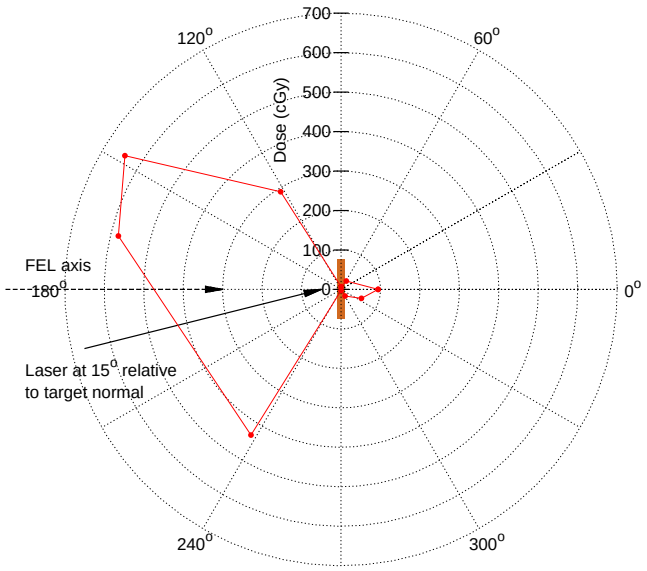

Figure 4: Dose (cGy) from nanoDots inside MEC chamber at 30 cm ($I = 1.8 \times 10^{18}$ W/cm^2 for 540 shots)

complexity of energy and angular distributions of hot electrons and their implications on photon doses outside target chamber.

4.2 Radiation Levels Outside Target Chamber

Figure 5 shows the maximum photon and neutron dose rates (ambient dose equivalent) measured above background with the active instruments outside the MEC chamber, excluding PTW pressurized ion chambers. Each BF_3 station also included a Victoreen 451 to measure photon dose rate at that location. All active detectors performed well at the laser intensity of 1.8×10^{18} W/cm^2 at 1 Hz and were not affected by any electromagnetic pulse effects as experienced at experiments elsewhere [14].

The maximum photon dose rate outside the target chamber of 60 μSv/h was measured by Victoreen #1 in the backward direction of the laser. This location outside the chamber corresponds with the mostly backward-directed nanoDot doses shown earlier in Figure 4. On the other hand, Victoreen #2 was shielded by 12 cm of steel shielding inside the chamber and did not measure greater than background during the experiment. This result demonstrates the effectiveness of localized shielding (designed for up to $\sim 10^{20}$ W/cm^2 and 8 J) inside the target chamber for a laser intensity of 1.8×10^{18} W/cm^2.

The photon dose rates from active detectors outside the MEC chamber in Figure 5 agree well. Differences between the photon dose rates may be due to self-shielding effects of the optics equipment and lenses inside the chamber as seen earlier in Figure

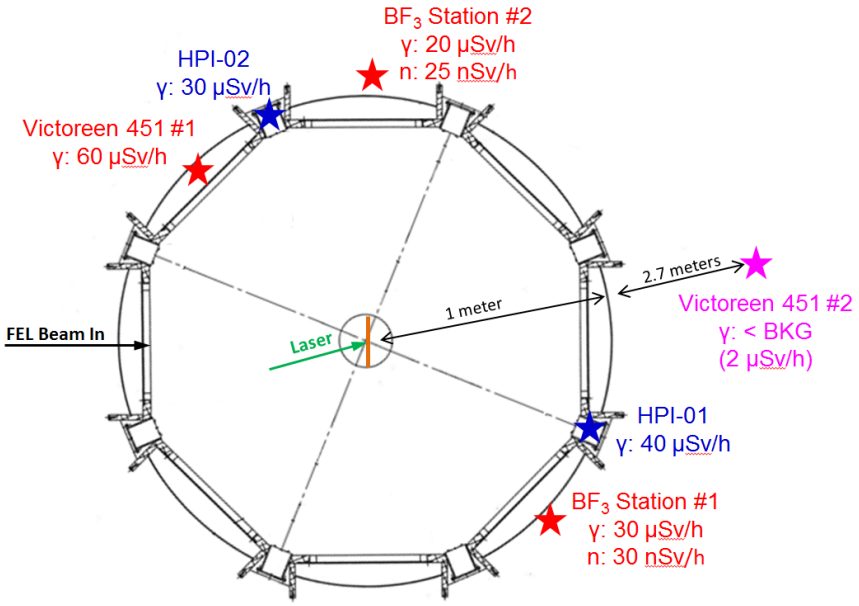

Figure 5: Maximum dose rates from active detectors at target chamber ($I = 1.8 \times 10^{18}$ W/cm^2 at 1 Hz)

3. Comparing results from active detectors suggest the photon dose rate outside the MEC chamber is directionally dependent and dependent on the dose inside the chamber. PTW-01 was located inside the Hutch 6 control room above the hutch roof. The control room is 3 m above the MEC target chamber and shielded by about 25 cm of concrete roof. This combination of distance and shielding caused PTW-01 to only measure a maximum dose rate of 0.01 μSv/h above background. PTW-02 was located outside the Hutch 6 steel roll up door about 6 meters from the target chamber and measured a maximum dose rate of 0.1 μSv/h above background.

Figure 6 shows a marked drop in photon dose rates over the course of 540 laser shots at 1 Hz. The same decreasing pattern was also observed by the BF_3 neutron detectors. The left bunch represents 140 shots, and right bunch represents 400 for a total of 540 laser shots on the copper target with a starting peak intensity of 1.8×10^{18} W/cm^2. The drop in dose rates is linked with the progressive damage of the Al-coated OAP focusing mirror. In addition, the sudden dips in the dose rate are due to the target rastering system shifting the copper foil to provide fresh material for laser shots.

Most passive dosimeters such as the 2 mSv PIC, InLight, and Luxel+ that measure integrated dose were not sensitive enough and did not read above background. Measurements with more sensitive dosimeters (RADOS and 0.02 mSv PIC) did provide dose results that agreed well with each other. The maximum integrated doses

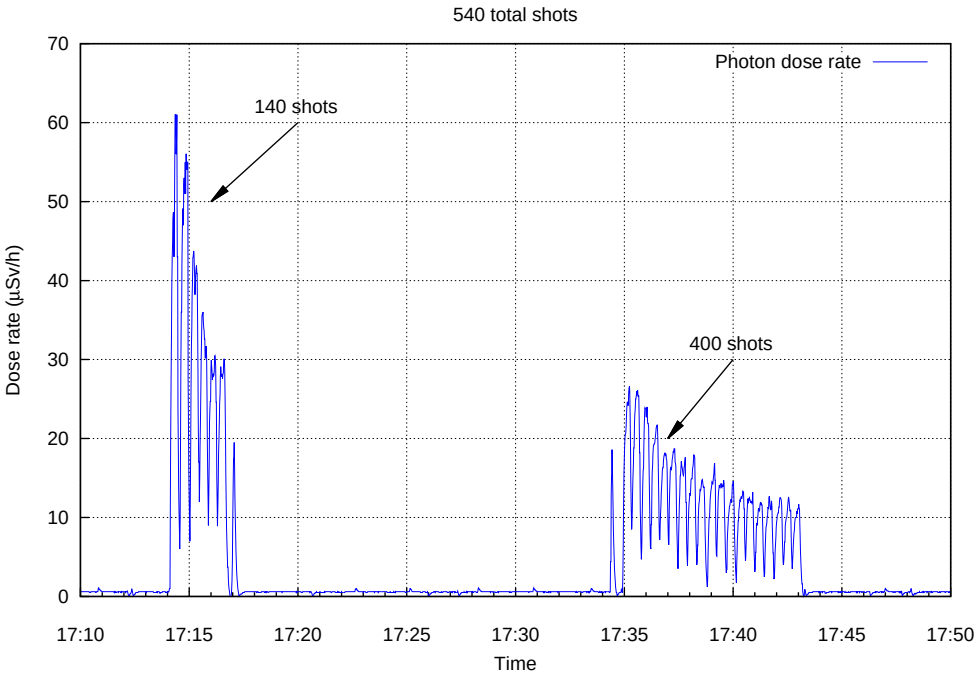

Figure 6: Photon dose rates from Victoreen 451 #1

measured on the passive dosimeters outside the target chamber were 4 μSv around the sides and 6 μSv above the chamber roof. The passive dosimeters on the roof measured higher doses because the chamber roof is thinner than the sides.

4.3 Photon Dose Yield

Figure 7 presents the maximum measured dose yield from this and two past experiments [14, 16], and error bars represent one standard deviation. Dose yield (ambient dose equivalent generated per laser shot energy) is in units of mSv/J at a distance of 1 meter. The blue triangles are from the 2012 MEC experiment [16], and the purple pluses are the 2011 measurements performed by SLAC RP at the LLNL Titan laser facility [14]. The Titan results are shown with no error bars, since they were obtained parasitically from another experiment, and thus the laser-optic parameters were not well characterized and subject to large uncertainties.

The three green circles are measurements from the February 2014 MEC experiment presented earlier and represent detector locations outside the target chamber wall (5.08 cm Al). The right point at 1.8×10^{18} W/cm^2 is the dose yield generated from the peak laser intensity before OAP mirror damage. The left point at about 1.1×10^{18} W/cm^2 is the final intensity inferred from the drop in dose rate observed in Figure 6. This laser intensity is calculated assuming the energy transmission fraction

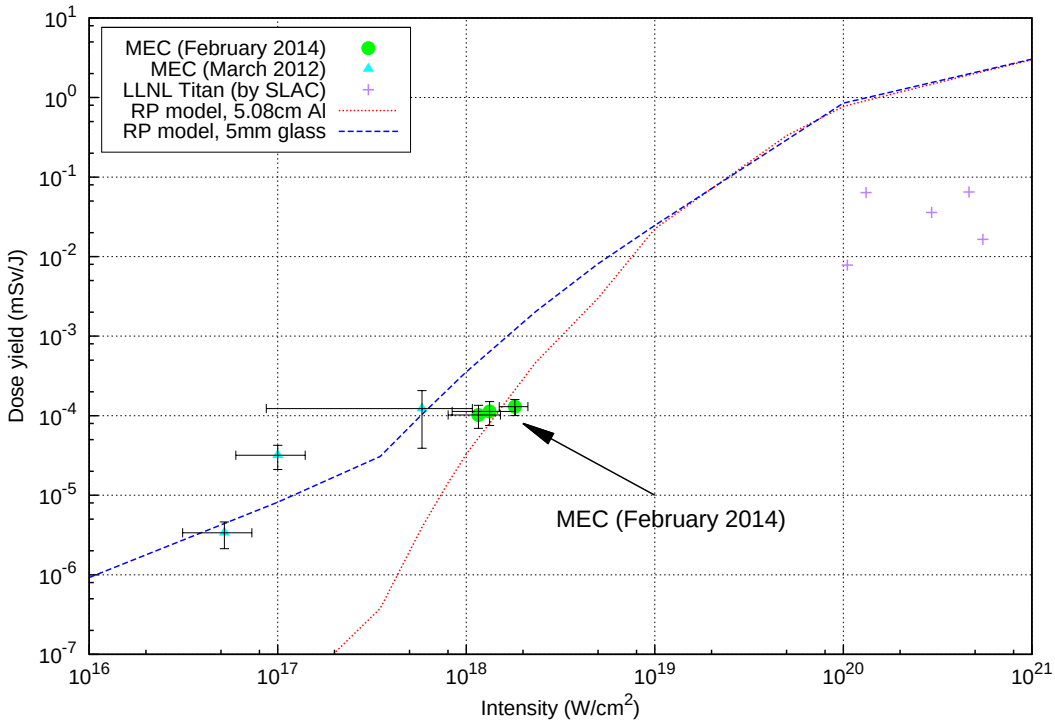

Figure 7: Photon dose yield (mSv/J) at 1 meter

of the OAP mirror decreases proportionally with the observed decrease in dose rate. The middle point is associated with the integrated dose measurements by passive dosimeters and is a shot-weighted average of the two other laser intensities.

The two lines for the RP model represent the analytical calculation of photon dose as described earlier. The MEC target chamber is primarily Al wall with thin glass viewports. The dashed blue line estimates the photon dose yield through the thin 5 mm glass viewport of the MEC target chamber. Similarly, the dotted red line estimates the photon dose yield transmitted through a 5.08 cm thick Al chamber door. After converting the dose rates and integrated doses measured by active and passive instruments from earlier, the dose yield around the outside of the MEC target chamber is about 10^{-4} mSv/J. This is in agreement with the RP model adjusted for attenuation of 5.08 cm of aluminum wall.

4.4 Neutron Dose Outside Target Chamber

As seen earlier in Figure 5, the results of the two BF_3 neutron detectors agreed with each other, measuring a maximum neutron dose rate of 30 nSv/h. The neutron dose rate also translates to a dose yield of about 5×10^{-8} mSv/J at 1 m and a neutron-to-

photon yield fraction of about 2×10^{-3} for $I = 1.8 \times 10^{18}$ W/cm^2. Figure 8 compares the neutron results from the February 2014 MEC experiment to other experiments where neutrons were also measured [16, 20].

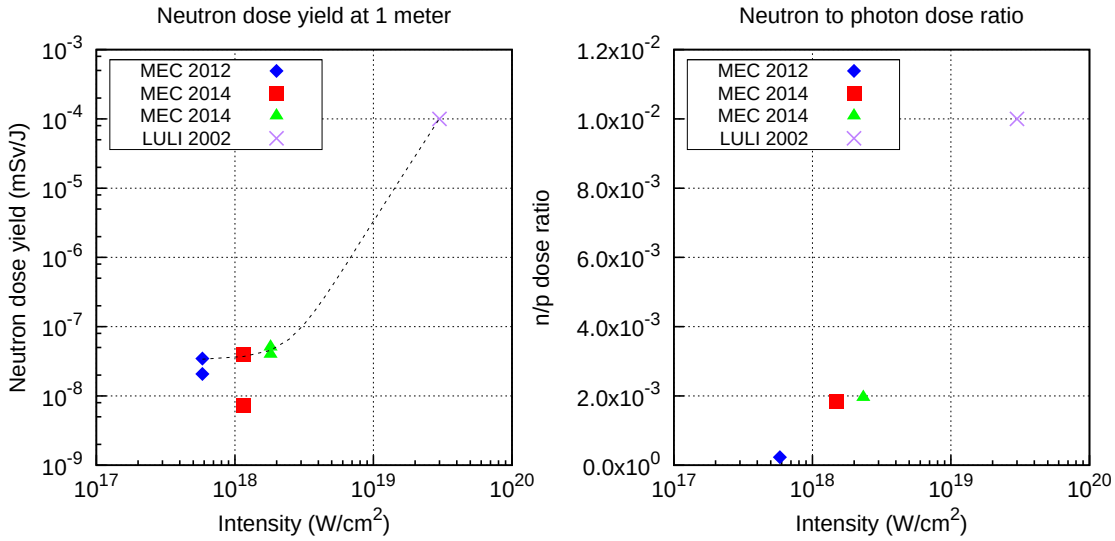

Figure 8: Neutron measurements from SLAC and LULI [20]

5 FLUKA Simulations

Monte Carlo simulations with the radiation transport code FLUKA were used to calculate the bremsstrahlung photon yield outside the MEC target chamber from hot electron interactions inside the chamber and to compare with experimental measurement results. FLUKA2011 Version 2b.5 was used for all simulations [26–28]. The energy thresholds for electron and photon production and transport in FLUKA were both set at 1 keV.

5.1 Electron Source Term

The information on angular distribution of the electrons source term is limited. Thus, two opposite scenarios for the electron angular distribution were considered in the FLUKA simulations: mono-directional and isotropic.

For the mono-directional case, the electron source is modeled as a pencil beam and directed along the path of the laser. The electron beam (with energy sampled from a distribution characterized by Equation 4 and T_h from Equation 2) interacts with the laser target (100 μm thick copper foil). Figure 9 shows the FLUKA-calculated one-dimensional ambient dose equivalent H*(10) yield projected along the direction

of the mono-directional electron beam (+x axis). The asymmetrical 1-D dose profile is a result of the simulated mono-directional electron pencil beam interacting with the copper target at x=0 cm. The 12 cm local steel shields at x=±40 cm effectively reduce the ambient dose (mixed electron and photon field) by at least two orders of magnitude, and the Al walls of the chamber itself serve to further reduce the dose (dominated by photons) that may escape the target chamber.

For the isotropic beam case, the electrons are again sampled from an energy distribution characterized by Equation 4, but instead of being modeled as a pencil beam like the mono-directional case, the electrons are emitted isotropically as a point source from the surface of the copper target.

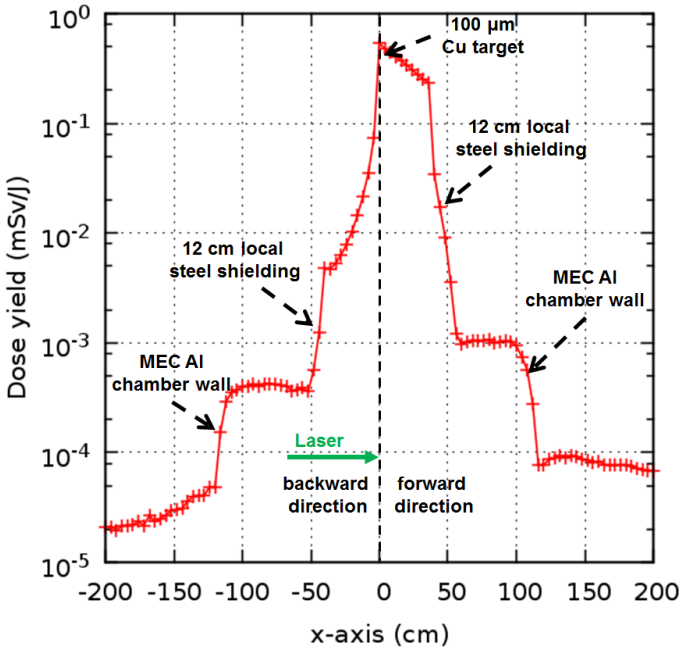

Figure 9: 1-D total ambient dose equivalent H*(10) projection ($I = 1.8 \times 10^{18}$ W/cm^2, T_h=183 keV, mono-directional)

5.2 Source of Dose Outside Target Chamber

Simulations in FLUKA are used to gain additional insight on where the photon dose measured outside the MEC target chamber during the experiment originates from. Figure 10 presents results from two separate FLUKA simulations where bremsstrahlung photon production was suppressed in either the Al chamber wall or the Cu target using a high energy (1 GeV) threshold for photon production. In Figure 10, the dose map on the left shows the total ambient dose equivalent for the target chamber when there is no bremsstrahlung photon production in the Al walls. The dose map on the

right shows the ambient dose equivalent when there is no bremsstrahlung production in the Cu target. For both scenarios, the ambient dose equivalent inside the target chamber remains relatively unchanged because of dominance of electrons.

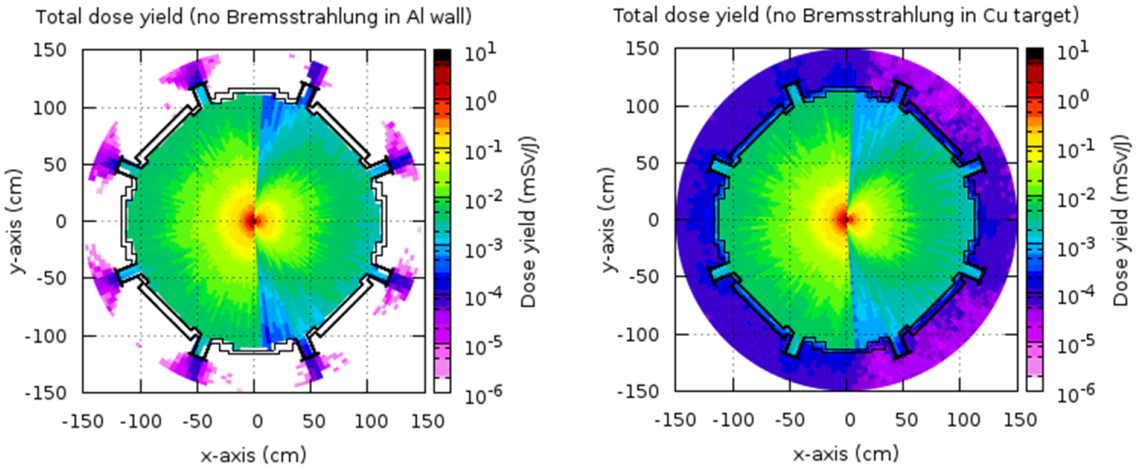

Figure 10: Suppression of bremsstrahlung photon production in FLUKA ($I = 1.8 \times 10^{18}$ W/cm^2, T$_h$=183 keV, isotropic)

The comparison in Figure 10 appears to indicate that dose outside the MEC target chamber is dominated by bremsstrahlung photons from electron interactions with the Al chamber wall for $I = 1.8 \times 10^{18}$ W/cm^2. When photon production is suppressed in the Al walls, only a slight amount of dose escapes the chamber via the thin glass viewports. Whereas when bremsstrahlung is suppressed only in the target, the dose is seen all around the outside of the target chamber and agrees well with photon yield measured by the active instruments. This is especially noticeable in the backward (–x axis) direction outside the chamber where the dose is about 10^{-4} mSv/J.

Figure 11 shows the 1-D dose yield projection for electrons and photons when simulating either a mono-directional or isotropic electron beam scenario in FLUKA with energy thresholds of 1 keV for both electrons and photons. The 1-D slice is in the backward direction, extending radially from the laser-target interaction point at R=0 cm. As before, the target is a 100 μm thick copper foil. Also, the FLUKA calculation did not implement any local steel shielding inside the target chamber because measurement locations of interest were unshielded during the actual experiment.

When observing a 1-D slice in the backward direction, the electron and photon dose yields differ between the isotropic or mono-directional electron beam scenarios. For an isotropic electron beam in FLUKA, the electron dose contribution dominates over the photon. However, this relation is reversed for a mono-directional source where the photon dose is greater. This behavior is expected due to the fact that source electrons are emitted in all directions, including backwards, for the isotropic

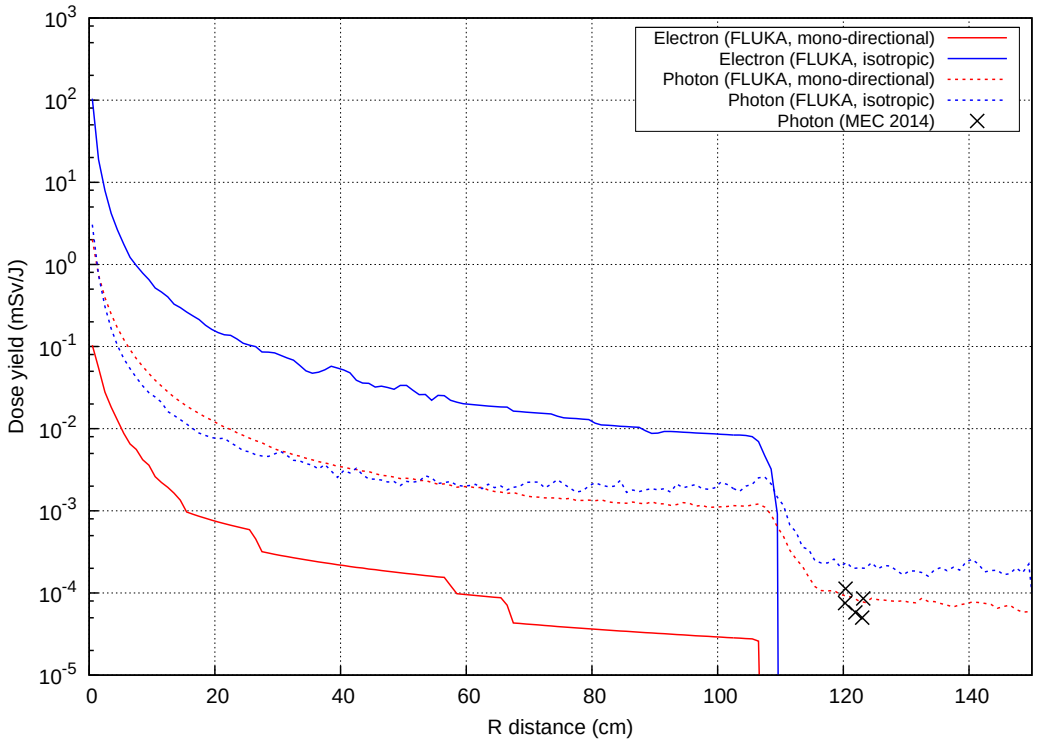

Figure 11: Comparison of 1-D FLUKA H*(10) projection with measured photon dose ($I = 1.8 \times 10^{18}$ W/cm^2, T_h=183 keV)

case, and only in the forward direction for the mono-directional case. Thus, the electron dose seen in Figure 11 for the mono-directional case is primarily due to back-scattered electrons from interactions with the copper target, whereas both source electrons and scattered electrons contribute to the electron dose in the backward direction for an isotropic electron beam scenario.

On the other hand, bremsstrahlung photons from electrons interacting with the copper target or aluminum chamber is the dominant mechanism that contributes to the photon dose yield for both electron beam direction scenarios, but a few interesting observations can be made from their slight differences in Figure 11. Inside the chamber at about R<50 cm, the photon yield from a mono-directional source is greater than the yield from an isotropic source because all the mono-directional source electrons in FLUKA can experience bremsstrahlung with the copper target. Near the Al chamber wall (R=100 cm), the photon yield is greater for the isotropic case due to source electrons now interacting with the Al chamber wall and producing bremsstrahlung photons. Photon build-up in the chamber wall can even be observed for the isotropic case at about R=105 cm. The photon dose outside the MEC chamber (R>110 cm) is also greater for the isotropic case.

Active and passive instruments measured photon dose yields of about 10^{-4} mSv/J outside the MEC target chamber. As seen in Figure 11, these experimental results agree well with the 1-D ambient dose equivalent projection calculated in FLUKA simulations.

6 Summary

As part of an on-going study, recent experiments at SLAC MEC focused a high intensity laser (1.8×10^{18} W/cm^2, T_h=183 keV, 0.2 J at 1 Hz) onto 100 μm thick copper targets. Active and passive detectors measured the ionizing radiation generated inside and outside the target chamber. Preliminary results show photon and neutron dose yields of around 10-4 and 5x10-8 mSv/J, respectively, outside the MEC target chamber. Inside the chamber, passive dosimeters measured very high integrated doses, primarily due to low energy electrons, up to 650 cGy after 540 laser shots. Analysis of the complex electron source term and mixed electron/photon dose results inside the chamber are ongoing, and particle-in-cell plasma code studies are planned to better characterize the energy and angular distribution of the electron source term generated from the laser plasma.

Analytical models appear to provide a good estimate of the photon dose yield outside the target chamber generated from laser-matter interactions Measurements of photon H*(10) outside the MEC target chamber also agree with results of FLUKA simulations. Future plans are underway at SLAC to further upgrade the MEC laser to a pulse energy of 8 J, and dedicated radiation measurements at higher laser intensities up to 2×10^{20} W/cm^2 (T_h=3.5 MeV) with different targets (including gas acceleration) will be performed.

ACKNOWLEDGEMENTS

This work was supported by Department of Energy under contract DE-AC02-76–SFO0515. The authors wish to acknowledge support from William White (SLAC), Philip Heimann (SLAC), and Thomas Cowan (HZDR).

References

[1] J. Hastings *et al.*, LCLS RPD SP–391–001–89 R0, (2009).

[2] W. P. Leemans *et al.*, Nat. Phys. **2**, 696 (2006).

[3] T. Tajima and J. M. Dawson, Phys. Rev. Lett., **43**, 267 (1979).

[4] G. Malka and J. L. Miquel, Phys. Rev. Lett. **77**, 75 (1996).

[5] F. Brunel, Phys. Rev. Lett. **59**, 52 (1987).

[6] S. C. Wilks *et al.*, Phys. Rev. Lett. **69**, 1383 (1992).

[7] S. C. Wilks and W. L. Kruer, IEEE J. Quantum Electron. **33**, 1954 (1997).

[8] F. Amiranoff *et al.*, Phys. Rev. Lett. **81**, 995 (1998).

[9] M. I. K. Santala *et al.*, Phys. Rev. Lett. **84**, 1459 (2000).

[10] T. Guo *et al.*, Rev. Sc. Instr. **72**, 41 (2001).

[11] L. M. Chen *et al.*, Phys. Plasmas **11**, 4439 (2004).

[12] R. Qiu *et al.*, SLAC RP Note RP–10–11, (2010).

[13] R. Qiu *et al.*, SLAC–PUB–14351, (2011).

[14] J. Bauer *et al.*, SLAC RP Note RP-11-11, (2011).

[15] M. Woods, SLAC LSO Memo 2010–10, (2010).

[16] J. Bauer *et al.*, SLAC PUB–15889, (2013).

[17] D. D. Meyerhofer *et al.*, Phys. Fluids B **5**, 2584 (1993).

[18] H. Chen *et al.*, Phys. Plasmas **16**, 020705 (2009).

[19] P. Mulser and D. Bauer, *High Power Laser-Matter Interaction*, Springer, Berlin Heidelberg, 416 p, (2010).

[20] F. Borne *et al.*, Radiat. Prot. Dosim. **102**, 61 (2002).

[21] K. W.D. Ledingham *et al.*, Phys. Rev. Lett. **84**, 899 (2000).

[22] M. D. Perry *et al.*, Lawrence Livermore National Laboratory UCRL–ID–129314, (1997).

[23] Y. Hayashi *et al.*, Radiat. Prot. Dosim. **121**, 99 (2006).

[24] M. H. Key *et al.*, Phys. Plasmas **5**, 1966 (1998).

[25] Y. Ping *et al.*, Phys. Rev. Lett. **100**, 085004 (2008).

[26] "The FLUKA code: Description and benchmarking" G. Battistoni, S. Muraro, P.R. Sala, F. Cerutti, A. Ferrari, S. Roesler, A. Fassò, J. Ranft, Proceedings of the Hadronic Shower Simulation Workshop 2006, Fermilab 6-8 September 2006, M. Albrow, R. Raja eds., AIP Conference Proceeding 896, 31–49, (2007).

[27] "FLUKA: a multi-particle transport code" A. Ferrari, P.R. Sala, A. Fassò, and J. Ranft, CERN-2005-10 (2005), INFN/TC_05/11, SLAC-R-773.

[28] V. Vlachoudis "FLAIR: A Powerful But User Friendly Graphical Interface For FLUKA" Proc. Int. Conf. on Mathematics, Computational Methods & Reactor Physics (M&C 2009), Saratoga Springs, New York, (2009).